

静止轨道全谱段宽覆盖成像光谱仪光学系统设计 与高保真分光系统研制

朱嘉诚^{1,2}, 赵知诚^{1,2}, 刘全^{1,2*}, 陈新华^{1,2}, 李欢³, 唐绍凡³, 沈为民^{1,2**}¹苏州大学光电科学与工程学院, 江苏 苏州 215006;²江苏省先进光学制造技术重点实验室 & 教育部现代光学技术重点实验室, 江苏 苏州 215006;³北京空间机电研究所, 北京 100094

摘要 根据静止轨道特点, 分析设计覆盖近紫外至长波红外波段的成像光谱仪光学系统, 将0.3~12.5 μm的光学全谱段细分为5个子谱段并集成于光学系统, 每个子谱段均采用4个分光系统在视场内拼接实现宽幅所需的超长狭缝, 狹缝总长最长达241.3 mm, 通过内扫描实现400 km×400 km地面覆盖。重点研究满足拼接要求的紧凑型长狭缝分光系统, 指出其实现高保真分光成像需满足低畸变、低杂散、高信噪比、均匀光谱响应等条件。据此, 设计基于凸面闪耀光栅的Offner型和Wynne-Offner型高保真分光系统, 并研制各个子谱段的原理样机。给出全谱段长狭缝和凸面闪耀光栅两种核心元件的研制结果, 单条狭缝最长达61.44 mm, 5个谱段的光栅槽密度范围为8.8~312.1 lp/mm, 峰值效率均在70%以上, 最高达86.4%。以可见近红外和长波红外两个谱段为例, 给出分光系统装调和测试过程, 结果表明所研制的分光系统具有高保真性能, 各项指标均满足要求。

关键词 光学设计; 成像光谱仪; 全谱段; 高保真; 静止轨道; 凸面闪耀光栅

中图分类号 TH74

文献标志码 A

DOI: 10.3788/AOS221884

1 引言

成像光谱仪可同时采集目标空间信息和光谱信息, 具有图谱合一的优势。经20世纪80—90年代的发展, 一系列成像光谱仪被研制成功并在航空平台获得广泛应用^[1-6]。进入21世纪, 该技术被应用到航天领域并在星载高光谱遥感领域得到快速发展。自2000年对地观测卫星EO-1携带首台星载高光谱成像仪Hyperion^[7]以来, 已有诸多卫星搭载或计划搭载成像光谱仪开展对地观测任务, 在海洋和海岸带检测^[8-11]、环境监测^[12]、地表探测^[13-15]、资源勘探^[16]、军事活动^[17]等应用中发挥作用。高光谱遥感方法^[18-21]和系统^[22-25]也得到快速发展。各领域对高效获取精准地物图谱信息的需求日益增长, 驱使高光谱遥感仪器往更快响应、更大幅宽、更高分辨率、更高信噪比的方向发展。位于地球静止轨道的卫星具有和地面保持相对静止的独特优势, 其对地观测具有高时效性和持续观测优势, 能快速、大范围获取地物目标信息。目前, 在静止轨道上服役的对地观测全谱段光谱类遥感载荷均为多光谱载荷^[26-29], 从紫外到长波红外的全谱段范围只有十几个

光谱通道, 不足以获取地物目标的指纹信息, 辨别目标物种种类和成分的能力远不如高光谱载荷。而关于静止轨道高光谱载荷的研究局限在单个或一些特殊谱段, 集中在大气监测等应用^[30-36]。近紫外、可见光和短波红外融合中长波红外的高光谱数据, 可极大提升目标识别精度和科学描绘维度, 并兼备全天候观测能力。但由于此类高光谱载荷研制难度大、成本高, 目前少有相关研究报道。在地球静止轨道获取大范围的全谱段精细地物光谱信息, 特别是定量化的高分辨率光谱数据, 是国际航天高光谱探测领域的技术制高点。为了充分满足环境、农业、林业、海洋、气象和资源等领域对全天时大范围连续监测、精细识别和分类的应用需求, 必须发展静止轨道全谱段高光谱探测技术, 这也是航天高光谱遥感的发展趋势。

本文提出一种全谱段、宽覆盖、高空间分辨率的光学系统, 在阐明其工作原理的基础上, 给出光学系统设计方案并分析其性能。重点研究各子谱段分光系统, 分析它们实现高保真光谱成像的难点和要求, 研制了各子谱段分光系统原理样机并进行了测试。

收稿日期: 2022-10-26; 修回日期: 2022-11-21; 录用日期: 2022-11-25; 网络首发日期: 2023-01-04

基金项目: 国家重点研发计划(2021YFD2000101, 2016YFB0500501)、国家自然科学基金(62105230)、中国博士后科学基金(2020M681700)

通信作者: *liuquan@suda.edu.cn; **swm@suda.edu.cn

2 工作原理与指标

静止轨道全谱段宽覆盖高保真成像光谱仪(GeoFWHIS)的指标要求和系统参数如表1和表2所示,该仪器覆盖的波长范围为0.3~12.5 μm,在大气窗口内可分为5个子谱段,包括B1(UVIS)、B2(VNIR)、B3(SWIR)、B4(MWIR)和B5(LWIR)。不同子谱段的空间分辨率、光谱分辨率、调制传递函数(MTF)、信噪比(SNR)、噪声等效温差(NETD)等指标不同,所用的探测器规格也不同,各子谱段须通过不同的光学通道进行分光成像,因此合理的系统布局尤为重要。位于静止轨道的载荷与地面保持相对静止,曝光时间不受平台运动限制,可通过主动延长曝光时间来获得足够的信噪比,从而降低光学系统对大相对孔径的需求。同时,因为载荷与地面保持相对静止,无法利用沿轨运动的特性进行推扫工作,GeoFWHIS采用系统内扫描的方式完成单景400 km×400 km覆盖范围的光谱成像。GeoFWHIS布局框图如图1(a)所示,其光学系统由1个无焦望远系统、3个成像物镜和5个子谱段的分光系统组成。无焦望远系统将大口径入射光束压缩成小口径平行光出射,在其出瞳处,扫描镜将压缩后的光束反射进入3个成像物镜,由分色镜将全谱段分为5个子谱段后再经分光系统

分光。通过扫描镜在无焦系统出瞳处的扫描,完成一景图像的高光谱数据提取,通过平台转动和姿态调整,指向下一景图像继续进行光谱成像,过程如图1(b)所示。这种布局方式的优点在于:扫描镜位于所有成像物镜前,可同时对其后全部子系统扫描成像;扫描镜位于无焦望远系统出瞳位置,前后都是平行光,扫描过程允许的容差大,具有高稳定性。

从表1和表2的数据可以看出,GeoFWHIS具有宽幅和高空间分辨率,B1和B2谱段有16000个空间采样点,瞬时视场角达0.7 μrad。宽幅和高空间分辨率的特点也导致系统必然有长狭缝,狭缝总长达241.3 mm,这对当前分光系统和探测器的研制带来了极大挑战。本实验采用分光系统视场内拼接的方式来覆盖超长狭缝,根据所选探测器规模,每个子谱段均采用4个分光系统拼接,在覆盖狭缝总长的同时,每两个相邻分光系统之间仍有一定视场搭接余量。

表1 GeoFWHIS指标要求与光学系统参数

Table 1 Specifications and system parameters of GeoFWHIS

Specification and parameter	Value
Orbital altitude	Geostationary orbit (~36000 km)
Swath width /(km×km)	400×400
Field of view /[(°)×(°)]	0.64×0.64
Entrance pupil diameter /m	3.2

表2 GeoFWHIS全波段的光学系统参数
Table 2 System parameters of GeoFWHIS at full-spectrum

Band	B1	B2	B3	B4	B5
Wavelength range /μm	0.3~0.56	0.55~1.01	1~2.5	3~5	8~12.5
Spatial resolution /m	25	25	50	50	100
Spectral resolution /nm	4	5	10	50	200
MTF	0.17	0.17	0.17	0.12	0.12
SNR	250	250	150	—	—
NETD /K	—	—	—	0.3	0.3
Focal length /m	21.6	21.6	17.28	17.28	8.64
F number	6.75	6.75	5.4	5.4	2.7
Detector resolution	4096×2048	4096×2048	2048×256	2048×256	1024×256
Pixel size /μm	15×15	15×15	24×32	24×32	24×32
Total length of slit /mm	241.3	241.3	193	193	96.5
Number of splicing spectrometers	4	4	4	4	4
Single slit length /mm	61.44	61.44	49.152	49.152	24.576

3 光学系统设计与分析

GeoFWHIS光学系统的设计难点在于:1)通过集成化系统实现全谱段宽覆盖的高光谱成像;2)设计出适用于拼接的长狭缝紧凑型分光系统。本节主要根据系统指标参数和布局方式设计光学系统,并给出各部分系统的设计方案和像质评价结果。

3.1 无焦望远系统

无焦望远系统的入瞳直径为3.2 m,视场为0.64°×0.64°。在无焦系统的入(出)瞳共轭面,折射率n(n')、口径D(D')和视场角w(w')的乘积为一个常数,即拉赫不变量J^[37]:

$$nDw = n'D'w' = J. \quad (1)$$

系统角放大率为出射视场角w'和入射视场角w的比值,同时也等于入瞳口径D与出瞳口径D'的比

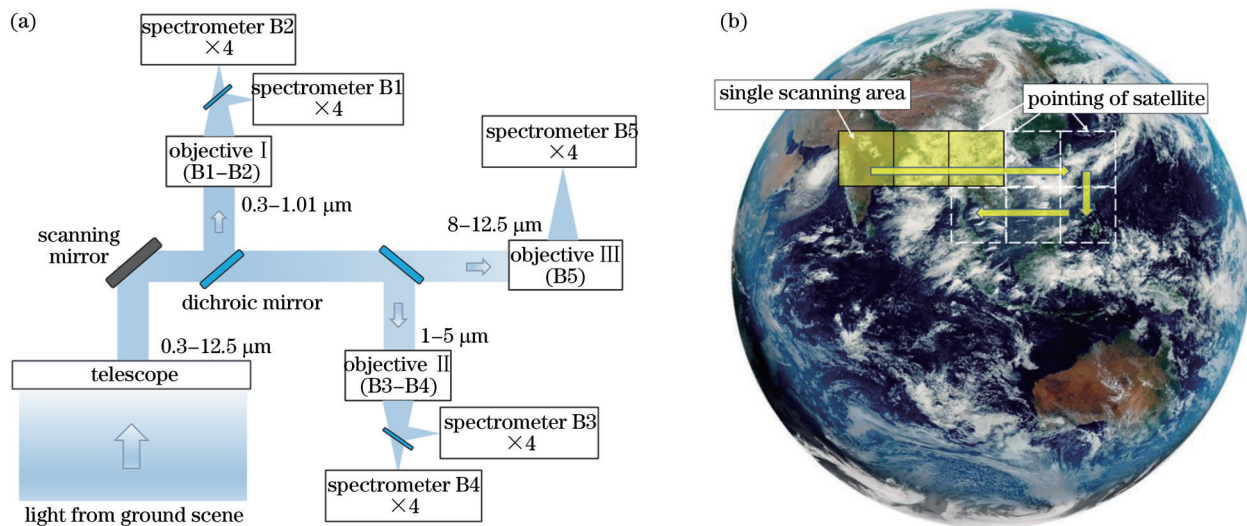


图1 GeoFWHIS工作原理示意图。(a)布局框图;(b)通过平台转动指向不同区域

Fig. 1 Working principle diagram of GeoFWHIS. (a) Layout diagram; (b) pointing to different coverages by turning the platform

值,即口径压缩比。因此口径压缩比越大,可得到越小的出瞳直径,但像方视场角会增大。尽管无焦系统的大压缩比可减小成像物镜的入瞳直径,但增大的视场角同样会导致成像物镜设计难度加大。结合以上分析,将口径压缩比确定为16,无焦系统的出瞳直径为200 mm,像方视场角为 $10.24^\circ \times 10.24^\circ$ 。

由于系统口径大,无焦望远系统采用反射式系统。在反射式无焦系统中,两反系统^[38]适用于小视场小放大率的应用场景,难以满足压缩比为16的要求;三反系统^[39]具有紧凑的结构和大视场,可实现高压缩比;四反系统^[40]具有更高的设计自由度,较三反系统具有更长的出瞳距和更优的像质,但对于大口径的无焦系统来说,四反系统会过于庞大复杂。因此采用三反系统是合适的,传统的同轴三反系统易于装调,但存在二次遮拦,尤其在压缩比为16时,出瞳尺寸小,甚至会被完全遮蔽,如图2(a)所示。离轴三反系统能解决遮拦问题,如图2(b)所示,但对于大口径系统,存在离轴量

大、体积大、压缩比小、主镜加工困难等问题。在同轴三反系统的基础上,折轴三反系统保持了相似结构,将三块反射镜分别进行轻微偏心与倾斜,能够避开二次遮拦,引出出瞳,且除主镜外,次镜和三镜依然保持较小的口径,因此本实验选取折轴三反系统作为无焦望远系统结构,所设计的光学系统光路如图2(c)所示。其中主镜、次镜、三镜均采用二次曲面,可满足大压缩倍率的需求。主镜采用抛物面,用于控制球差;次镜为双曲面,用于控制球差和子午彗差的平衡;三镜采用接近抛物面的双曲面,用于控制子午彗差和像散的平衡。主镜中心开孔直径为700 mm,线遮拦系数为0.22。在系统中间像面前添加一块平面反射镜,用于折叠光路,减小系统长度,便于出瞳和成像物镜对接。该无焦系统的中心视场波前误差均方根(RMS)值为 0.024λ (波长 $\lambda=632.8$ nm),0.7视场波前差RMS值为 0.052λ ,边缘视场波前差RMS值为 0.073λ ,具有较好的波前质量。

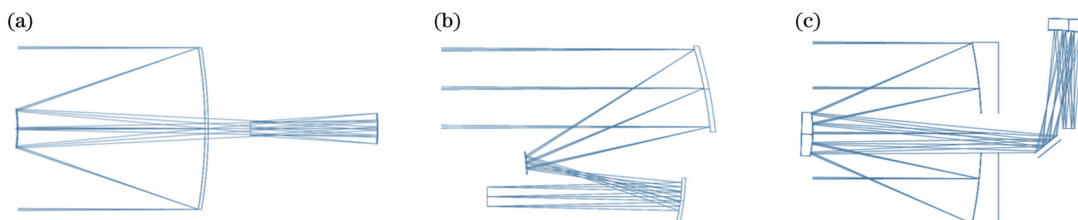


图2 三反无焦系统。(a)同轴三反;(b)离轴三反;(c)折轴三反

Fig. 2 Afocal three-mirror system. (a) Coaxial three-mirror; (b) off-axis three-mirror; (c) zigzag-axis three-mirror

3.2 成像物镜

将成像物镜对接在无焦望远系统之后,需要实入瞳与望远系统的出瞳匹配,各通道成像物镜的指标参数如表3所示,入瞳直径为200 mm,垂直扫描方向的视场角为 10.24° ,沿扫描方向也有较小视场,便于像处分光系统的狭缝拼接。成像物镜的焦距仅为

GeoFWHIS系统整体焦距的1/16,作为分光系统的前置物镜,通常需要满足像方远心成像要求。

考虑视场大小、谱段宽度、入瞳直径、质量与成本等因素,3个通道的成像物镜均采用离轴反射式系统。图3(a)所示的离轴两反系统可实现较大的视场角,孔径光阑位于主镜之后,为虚光阑,可实现像方远心成

表3 各通道成像物镜的指标参数
Table 3 Specifications of three objectives

Specification	Objective I	Objective II	Objective III
Wavelength range / μm	0.3~1.01	1~5	8~12.5
Entrance pupil diameter /mm	200	200	200
Field of view /[(°) \times (°)]	10.24 \times 0.22	10.24 \times 0.26	10.24 \times 0.53
Focal length /mm	1350	1080	540
F number	6.75	5.4	2.7

像。但该系统没有实入瞳,不便与无焦望远系统的出瞳对接,且在杂散光抑制方面不如具有实光阑的系统。**图3(b)**所示的有中间像面的三反系统中间实像位于次镜和三镜之间,可在其附近放置视场光阑来抑制一次杂光直接照射像面,具有较好的杂光抑制效果,但该系统很难获得像方远心的成像光束,不适合作为分光系统的前置物镜。无中间实像的离轴三反系统具有高成像质量,光阑可放在整个系统的前端,且可实现像方

远心成像,是GeoFWHIS成像物镜的优选结构。因此成像物镜均采用无中间实像的离轴三反系统,成像物镜I的光路如**图3(c)**所示,系统主镜和次镜均采用高次非球面,三镜采用二次椭球面,在成像光路中加入折叠镜,以减小系统总长,并将像面引到系统后方,便于和分光系统对接。成像物镜的像质接近衍射极限,远心度好、畸变小,主光线入射像面角度小于0.3°,畸变小于0.29%。

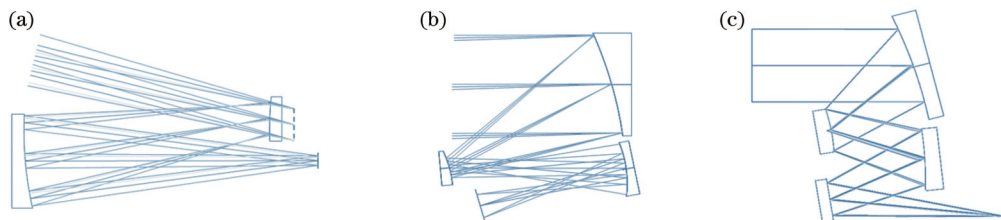


图3 离轴反射式成像系统。(a)两反系统;(b)有中间实像的三反系统;(c)无中间实像的三反系统

Fig. 3 Off-axis three-mirror imaging systems. (a) Two-mirror system; (b) three-mirror system with intermediate image; (c) three-mirror system without intermediate image

3.3 前置系统整体

由无焦望远系统和成像物镜构成GeoFWHIS的前置系统模型如**图4(a)**所示。系统中3个成像物镜分布在无焦望远系统主镜背部,3个成像物镜共入瞳,并与无焦系统的出瞳重合。扫描镜位于瞳面,将垂直于扫描方向的近视场光线反射进成像物镜,形成狭长像面。扫描镜摆动方向的视场被分时扫描进入成像物

镜,完成对扫描方向的视场覆盖,因此扫描镜需转动的角度为 $5.12^\circ \pm 2.56^\circ$,对应无焦系统 $0.64^\circ \pm 0.32^\circ$ 的物方视场和地面400 km的覆盖范围。**图4(b)、(c)**给出了扫描镜在两个极限扫描角度 $\pm 2.56^\circ$ 时的光路。在成像物镜I的像方光路中,通过分色镜将光束分为B1和B2两个谱段,在成像物镜II像方光路中分为B3和B4两个谱段,成像物镜III对应B5谱段。

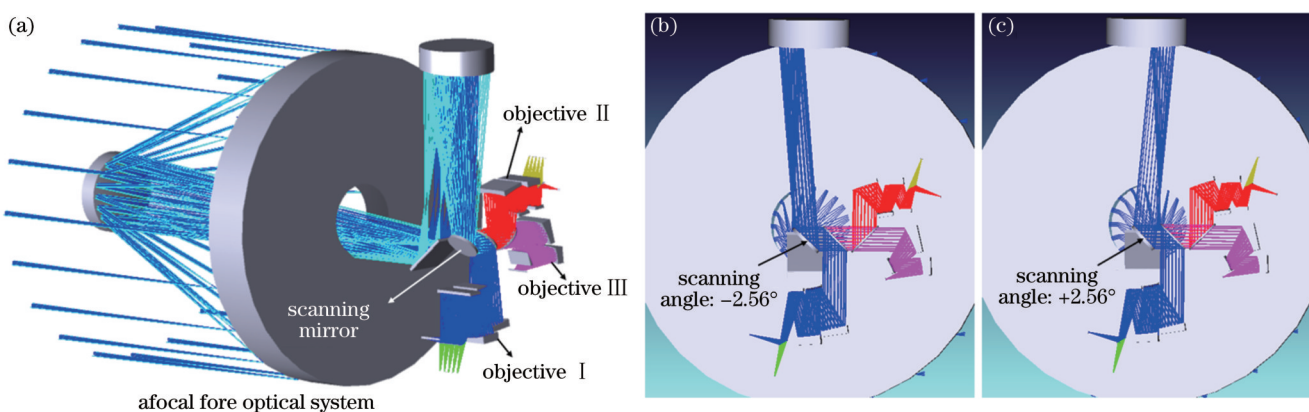


图4 前置系统的光路图。(a)前置系统三维模型;(b)扫描镜位于 -2.56° 边缘位置的光路;(c)扫描镜位于 $+2.56^\circ$ 边缘位置的光路

Fig. 4 Optical path of fore-optics system. (a) 3D model of fore-optics system; (b) optical path with scanning mirror at edge position of -2.56° ; (c) optical path with scanning mirror at edge position of $+2.56^\circ$

以B2通道为例,评价了前置系统在3个扫描角度下的成像质量。前置系统B2通道的MTF曲线和点列图如图5所示,当扫描角度为 -2.56° 和 0° 时,MTF接近衍射极限;当扫描角度为 2.56° 时,边缘视场的MTF略有下降,但像质仍较高。当扫描角度为

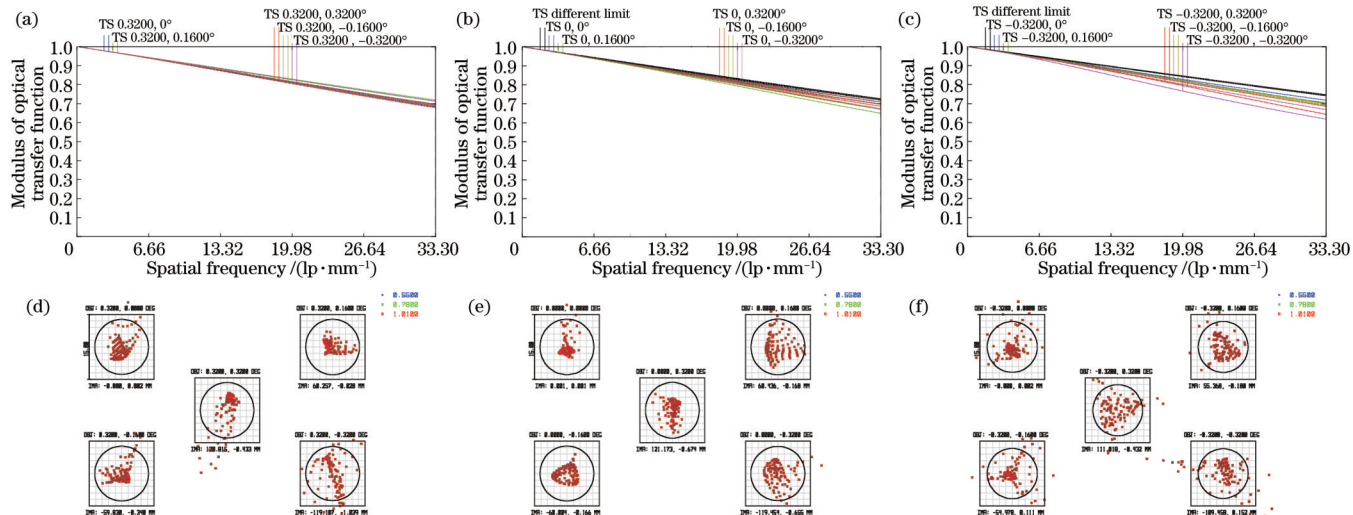


图5 B2谱段前置系统的MTF曲线和点列图。(a)~(c)扫描角为 -2.56° 、 0° 、 $+2.56^\circ$ 时的MTF曲线;(d)~(f)扫描角为 -2.56° 、 0° 、 $+2.56^\circ$ 时的点列图

Fig. 5 MTF curves and spot diagrams of fore-optics system in B2 band. (a)–(c) MTF curves with scanning angle of -2.56° , 0° , and $+2.56^\circ$; (d)–(f) sport diagrams with scanning angle of -2.56° , 0° , and $+2.56^\circ$

3.4 高保真分光系统

分光系统即光谱仪系统,是GeoFWHIS的核心模块之一,各谱段分光系统的指标参数已在表1和表2中给出,每个谱段均采用4个独立的分光系统模块通过“品”字形拼接覆盖狭缝总长,如图6所示。相邻两个分光系统的狭缝有一定搭接,拼接狭缝总长L与单个分光系统狭缝长度S和搭接量 δ_s 满足如下关系:

$$L = 4S - 3\delta_s \quad (2)$$

尽管采用视场内拼接的方式减小了单个分光系统的狭缝长度,但B1、B2谱段的狭缝仍然很长(61.44 mm),B3、B4谱段的狭缝长49.152 mm,B5谱段狭缝与前4个谱段相比较短。为避免同侧相邻两个分光系统干涉,单个分光系统在狭缝方向的宽度W必须满足如下条件:

$$W < 2S - 2\delta_s \quad (3)$$

这要求分光系统在长狭缝的情况下还要有极小的体积。

除了满足必要的几何尺寸要求,高保真的分光成像性能也是分光系统追求的目标^[41–42],这是实现高精度定量化高光谱遥感的关键。分光系统的诸多指标会影响其保真度,如MTF、SNR、光谱响应函数(SRF)、谱线弯曲(smile)、色畸变(keystone)、杂散光等。而在多个分光系统狭缝拼接方案中,保证分光成像性能在全狭缝范围的一致性尤为重要,这也是实现不同分光系统光谱图像高精度拼接的保障。目前,已有文献公

-2.56° 、 0° 和 $+2.56^\circ$ 时,奈奎斯特频率处的最低MTF值分别为0.68、0.67和0.61。从点列图可以看出,在各扫描位置处,点列图RMS半径均小于艾里斑半径,最大的点列图RMS半径为5.65 μm,小于单像元尺寸15 μm。

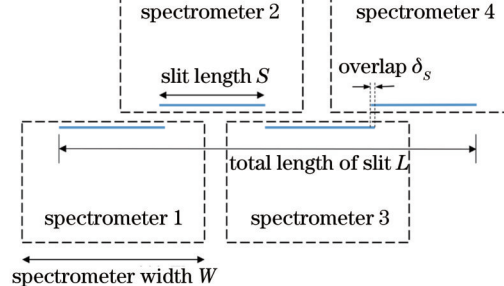


图6 分光系统拼接示意图

Fig. 6 Schematic of spectrometer splicing system

开报道了多种适用于长狭缝的分光系统结构,如图7所示,包括基于凸面光栅的Offner型分光装置^[43]及其改进的Wynne-Offner装置^[44–45]、自由曲面Offner装置^[46]、浸没式Offner装置^[47]、基于凹面光栅的Dyson型分光装置^[48]及由其改进的Wynne-Dyson装置^[49]、先进型Dyson^[50–51]装置,基于平面光栅和三反系统的R-T结构^[25],以及基于平面光栅的折反式系统CCVIS^[23]。这些结构在特定场景均有较优的分光成像性能,但并非都能满足超紧凑结构、高保真性能和适于拼接等要求。表4所示为各类分光装置的特征及性能,以及它们在长狭缝时的优缺点。

所设计的GeoFWHIS分光系统狭缝长、相对孔径小,需要十分紧凑的结构,并要有较长的前后工作距,便于拼接时光路折叠和探测器排布。考虑到上述需求

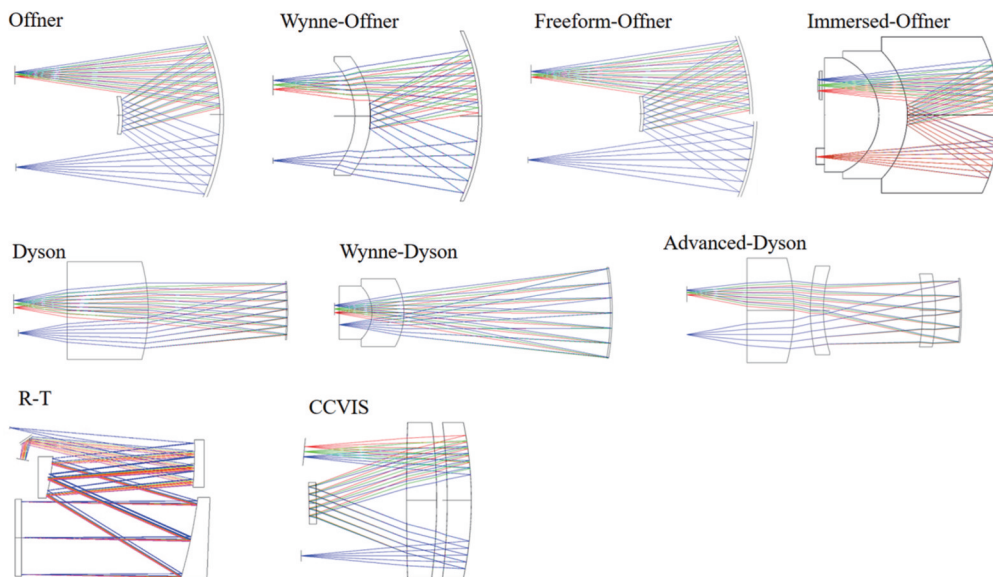


图7 不同分光系统光路图

Fig. 7 Optical path of different spectrometers

表4 不同分光系统优缺点对比

Table 4 Comparison of advantages and disadvantages for different spectrometers

Spectrometer type	Characteristic	Advantage	Disadvantage
Offner	• Convex grating; • Concentric structure	• Long working distance; • No smile and keystone	• Large volume with a long slit; • Residual astigmatism
Wynne-Offner	• A meniscus is added near the grating of Offner type	• Advantages of Offner type; • Anastigmatism; • Compact	• Additional polarization; • Hard to manufacture grating on meniscus
Freeform Offner	• Three freeform elements	• Advantages of Offner type; • Compact	• Extremely difficulty; • High cost
Immersed Offner	• Light travels in dielectric	• Advantages of Offner type; • Ultra-compact	• High cost; • High risk
Dyson	• Concave grating; • Concentric structure	• Large relative aperture; • No smile and keystone	• Large volume with a long slit; • Short working distance
Wynne-Dyson	• A meniscus is added behind the hemispherical lens of Dyson type	• Advantages of Dyson type; • Ultra-compact	• Short working distance
Advanced Dyson	• Several meniscus lenses added into the classic Dyson type	• Advantages of Dyson type; • Relatively long working distance	• Large volume with a long slit
R-T	• Double pass structure; • Plane grating; • Littrow mounting	• Compact; • Small distortion	• High cost; • Tight tolerance; • Small space between slit and image
CCVIS	• Catadioptric structure; • Immersed grating	• Long working distance; • Compact	• Residual keystone; • Thermal sensitive

和研制难度,B1、B2 和 B3 谱段采用 Wynne-Offner 分光装置,B4、B5 谱段采用经典 Offner 分光装置。国内外学者对 Offner 装置的像差理论和设计方法进行了较多研究^[52-54],关于 Wynne-Offner 装置的理论分析,本课题组也进行了详细报道^[55-56],本文不再赘述。所设计

的 5 个谱段分光系统的光路如图 8 所示,其结构与性能参数见表 5。

对分光系统的性能评价主要从影响其保真度方面展开,表 5 给出了部分性能,各谱段分光系统的谱线弯曲和色畸变均小于 1% 个像元,表明其具有极低的光

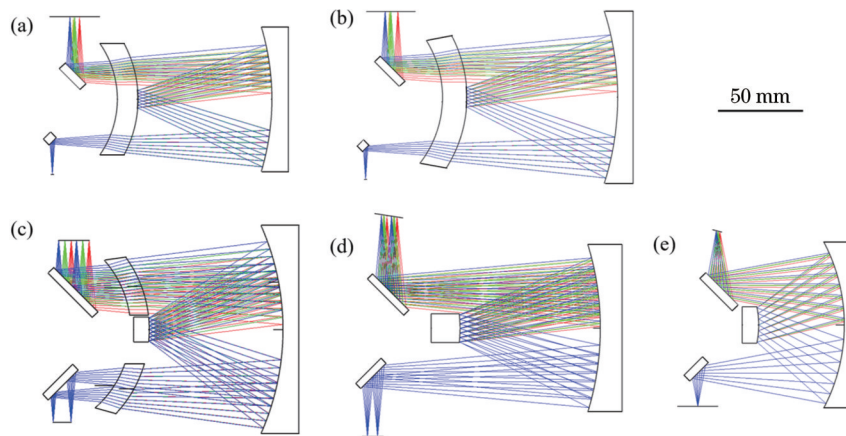


图8 GeoFWHIS分光系统光路图。(a) B1谱段;(b) B2谱段;(c) B3谱段;(d) B4谱段;(e) B5谱段

Fig. 8 Optical path of spectrometers in GeoFWHIS. (a) B1 band; (b) B2 band; (c) B3 band; (d) B4 band; (e) B5 band

表5 分光系统的主要特性参数

Table 5 System parameters and performance of spectrometers

Band	B1	B2	B3	B4	B5
Package size / (mm × mm × mm)	140×110×100	170×111×106	160×132×89	168×165×88	90×92×49
Smile /pixel	0.06%	0.11%	0.26%	0.31%	0.95%
Keystone /pixel	0.33%	0.47%	0.79%	0.42%	1.00%
MTF	0.86	0.77	0.72	0.41	0.28
Grating density /(lp·mm ⁻¹)	310	210	68	19.1	8.8
Blazed angle of grating /(^{\circ})	3.7	4.6	3.1	2.6	2.8

谱畸变,各谱段奈奎斯特频率处的MTF值接近衍射极限。各谱段SRF^[41]如图9所示。SRF描述分光系统对单位强度单色光的响应特性,是狭缝函数、线扩散函

数和探测器采样函数的卷积,高保真分光系统在不同视场处的SRF应保持一致。从图9(a)~(e)所示的SRF曲线可以看出,各谱段不同视场的SRF基本重

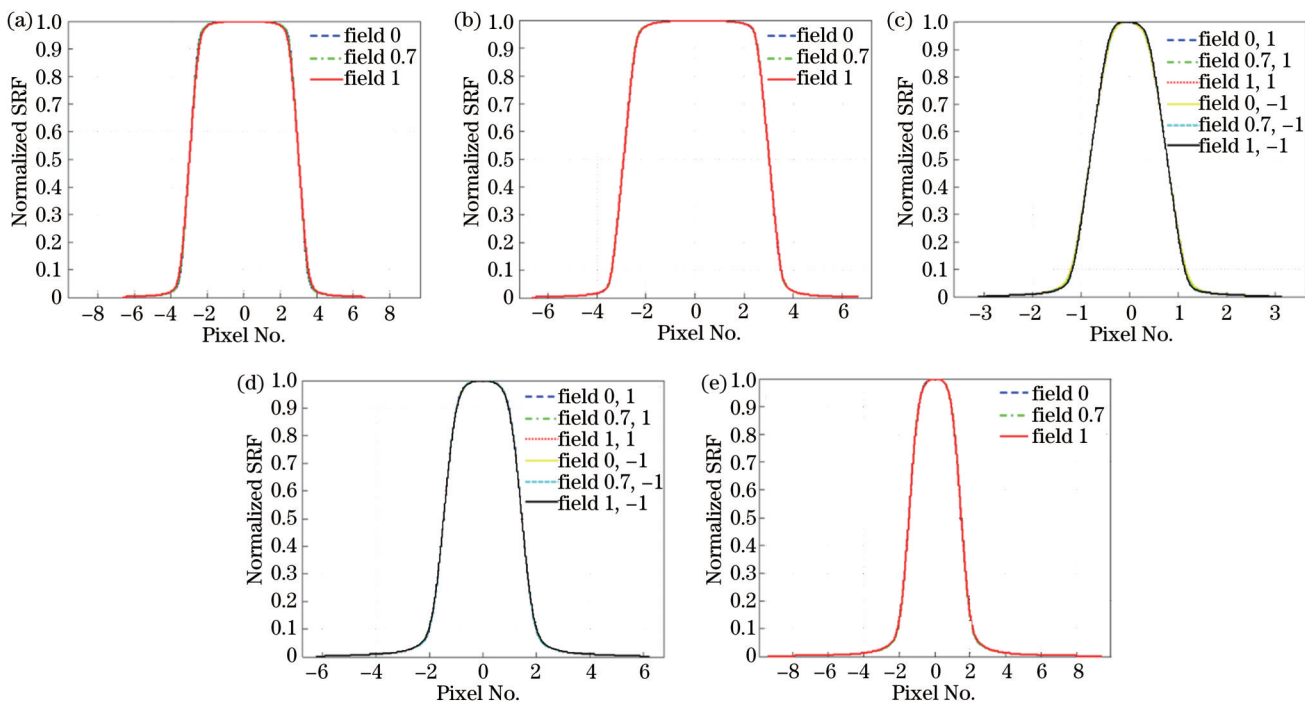


图9 各谱段分光系统的SRF。(a) B1谱段;(b) B2谱段;(c) B3谱段;(d) B4谱段;(e) B5谱段

Fig. 9 SRF of optical splitting systems for each band. (a) B1 band; (b) B2 band; (c) B3 band; (d) B4 band; (e) B5 band

合,表明分光系统的光谱均匀性良好。不同谱段的 SRF 曲线形状及半峰全宽(FWHM)存在差异,是因为光学系统线扩散函数、狭缝宽度和探测器像元尺寸、光谱过采样率不同。B1~B5 谱段光谱的过采样率分别为 6、6、1.6、3、3。

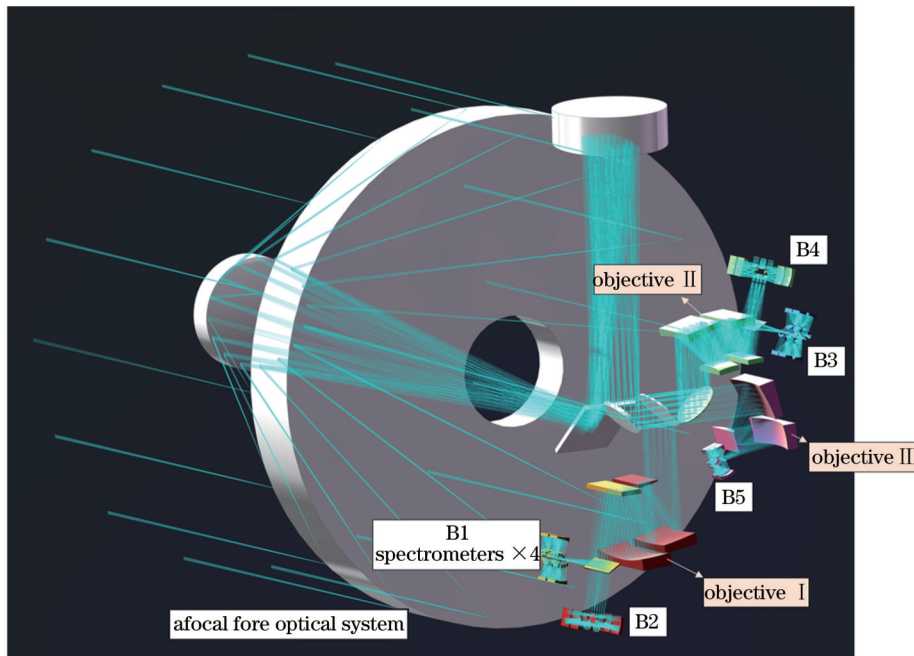


图 10 GeoFWHIS 光路示意图
Fig. 10 Lightpath diagram of GeoFWHIS

GeoFWHIS 的光谱性能由分光系统决定,已在第 3.4 节进行详细介绍。为充分评价 GeoFWHIS 的成像性能,需对系统处于不同扫描角度时,每一个分光系统在不同波长下的像质进行评价。本文给出每个分光系统在 3 个特征波长下、奈奎斯特频率处的 MTF 值,见表 6。可以看到:各分光系统 MTF 在扫描镜扫描角度为 0° 时具有最大值;当扫描角度为 ±2.56° 时,MTF 值有所下降,但仍满足指标要求。

信噪比是成像光谱仪探测极限和集光能力的重要体现,成像光谱仪高信噪比是获得高保真光谱数据的必要条件。信噪比定义为来自目标物的辐射在探测器光敏面上产生的有效信号电子数与噪声电子数的比值,表达式^[57]为

$$R_{SN} = \frac{S_{signal}}{N_{noise}} = \frac{S_{signal}}{\sqrt{N_{photon}^2 + N_{dark}^2 + N_{read}^2}}, \quad (4)$$

式中: S_{signal} 表示信号电子数; N_{noise} 表示噪声电子数;噪声主要包括光子散粒噪声 N_{photon} 、暗电流噪声 N_{dark} 和探测器读出噪声 N_{read} 。信号电子数表达式为

$$S_{signal} = B(\lambda)\tau(\lambda)Q(\lambda)t \frac{\pi ab}{4F^2} \frac{\lambda}{hc} m\Delta\lambda, \quad (5)$$

式中: $B(\lambda)$ 为入射光的光谱辐亮度; $\tau(\lambda)$ 为系统透过率; $Q(\lambda)$ 为探测器量子效率; t 为系统曝光时间; a, b 为探测器像元尺寸; F 为系统 F 数; m 为探测器像元合并

3.5 GeoFWHIS 光学系统整体

前文详细给出了 GeoFWHIS 各部分光学系统的设计方案和像质评价结果,本节将给出系统整体设计结果。GeoFWHIS 的光路示意图如图 10 所示,系统整体包络尺寸为 5.27 m × 3.45 m × 3.2 m。

数; $\Delta\lambda$ 为单个像元对应的光谱采样间隔; h 为普朗克常数; c 为真空中的光速。在近紫外至短波红外谱段,散粒噪声是主要噪声,是由探测器接收光子的涨落引起的,与接收光子数有关,可表示为接收光子数的平方根,即

$$N_{photon} = \sqrt{S_{signal}}. \quad (6)$$

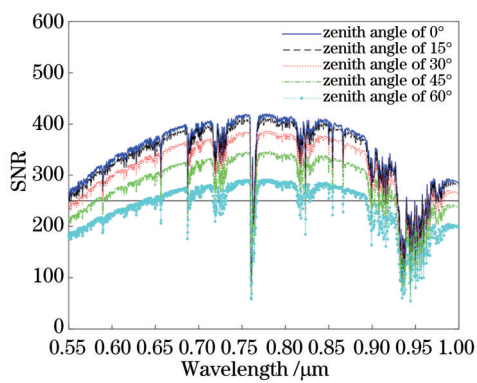
GeoFWHIS 可通过适当延长曝光时间 t 来提高信噪比,本文以 B2 谱段为例分析系统信噪比,所用 e2v 公司 CCD 探测器的饱和电子数为 200000,暗电流噪声为 140 electron/s,读出噪声为 12 electron/s,峰值量子效率为 85%。通过 Modtran 软件仿真获得入瞳辐亮度信息 $B(\lambda)$,由信噪比计算公式——式(4)计算得到,当积分时间为 80 ms,太阳天顶角小于 30° 时,信噪比小于 250,如图 11 所示。同样地,可计算得到 B1 谱段在积分时间为 110 ms,太阳天顶角小于 30° 时的信噪比小于 250;B3 谱段在积分时间为 100 ms 时,同等观测条件下可获得小于 150 的信噪比,满足指标要求。因此,完成 400 km × 400 km 单景图像高光谱数据采集所需的扫描时间至少为 30 min。

B4、B5 两个红外通道用 NETD 来表示对热辐射信号探测的灵敏度,NETD 的仿真计算方法详见文献[58]。经计算,当 B4 谱段分光系统的制冷温度为 160 K,探测 700 K 高温目标时 NETD 为 0.13 K,而当

表6 GeoFWHIS在奈奎斯特频率处的MTF数据

Table 6 MTF of GeoFWHIS at Nyquist frequency

Band	Serial number	Scanning angle of -2.56°			Scanning angle of 0°			Scanning angle of $+2.56^\circ$		
B1	Wavelength / μm	0.30	0.43	0.56	0.30	0.43	0.56	0.30	0.43	0.56
	Diffraction limit	0.88	0.84	0.80	0.88	0.84	0.80	0.88	0.84	0.80
	Spectrometer 1	0.80	0.76	0.75	0.80	0.79	0.77	0.60	0.59	0.57
	Spectrometer 2	0.82	0.79	0.76	0.82	0.80	0.78	0.77	0.72	0.66
	Spectrometer 3	0.81	0.79	0.77	0.85	0.79	0.78	0.75	0.71	0.63
	Spectrometer 4	0.73	0.69	0.67	0.78	0.74	0.72	0.61	0.58	0.53
B2	Wavelength / μm	0.55	0.78	1.01	0.55	0.78	1.01	0.55	0.78	1.01
	Diffraction limit	0.78	0.72	0.66	0.78	0.72	0.66	0.78	0.72	0.66
	Spectrometer 1	0.65	0.62	0.57	0.71	0.64	0.59	0.60	0.58	0.53
	Spectrometer 2	0.66	0.65	0.58	0.74	0.70	0.62	0.65	0.62	0.56
	Spectrometer 3	0.69	0.67	0.58	0.73	0.70	0.63	0.64	0.59	0.53
	Spectrometer 4	0.65	0.60	0.56	0.72	0.69	0.62	0.60	0.55	0.52
B3	Wavelength / μm	1.00	1.75	2.50	1.00	1.75	2.50	1.00	1.75	2.50
	Diffraction limit	0.84	0.74	0.63	0.84	0.74	0.63	0.84	0.74	0.63
	Spectrometer 1	0.69	0.63	0.55	0.72	0.60	0.54	0.63	0.55	0.40
	Spectrometer 2	0.79	0.70	0.62	0.81	0.70	0.65	0.69	0.62	0.51
	Spectrometer 3	0.77	0.70	0.61	0.80	0.71	0.65	0.77	0.69	0.55
	Spectrometer 4	0.78	0.71	0.61	0.79	0.68	0.63	0.78	0.66	0.54
B4	Wavelength / μm	3	4	5	3	4	5	3	4	5
	Diffraction limit	0.52	0.47	0.42	0.52	0.47	0.42	0.52	0.47	0.42
	Spectrometer 1	0.42	0.38	0.35	0.42	0.39	0.36	0.38	0.33	0.31
	Spectrometer 2	0.49	0.45	0.40	0.50	0.46	0.42	0.45	0.45	0.39
	Spectrometer 3	0.47	0.39	0.38	0.50	0.44	0.40	0.43	0.42	0.37
	Spectrometer 4	0.46	0.40	0.32	0.47	0.39	0.34	0.36	0.32	0.29
B5	Wavelength / μm	8.0	10.3	12.5	8.0	10.3	12.5	8.0	10.3	12.5
	Diffraction limit	0.35	0.31	0.27	0.35	0.31	0.27	0.35	0.31	0.27
	Spectrometer 1	0.28	0.25	0.22	0.31	0.26	0.25	0.29	0.25	0.23
	Spectrometer 2	0.31	0.27	0.23	0.32	0.27	0.24	0.31	0.27	0.24
	Spectrometer 3	0.30	0.26	0.23	0.31	0.27	0.26	0.30	0.26	0.22
	Spectrometer 4	0.29	0.25	0.24	0.30	0.26	0.23	0.30	0.25	0.22

图11 在晴朗无云的观测环境下,观测天顶角为 35° 、积分时间为80 ms时B2谱段的信噪比曲线Fig. 11 SNR curves for B2 band in cloudless environment when observation zenith angle is 35° and integration time is 80 ms

B5谱段分光系统的制冷温度为90 K,探测300 K常温目标时NETD为0.28 K,均满足指标要求。

4 分光系统样机研制与测试

4.1 核心元件

狭缝和光栅是分光系统的核心元件,研制高质量的狭缝和光栅是实现高保真分光成像的关键。狭缝作为视场光阑,其几何形状误差和刃口缺陷等会对系统光谱分辨率、光谱畸变、谱面均匀性产生不利影响。本实验研制的狭缝特点在于长度长、宽度窄,尤其是B1和B2谱段,单条狭缝长达61.44 mm,而宽度仅为15 μm ,长宽比超过4000,用传统的手工研磨、机械刻画、激光加工等方法很难保证狭缝的直线度、平行度和均匀性。本实验采用半导体工艺研制出各谱段硅基底的长狭缝^[56],如图12所示。通过步进光刻技术可严格

控制狭缝几何形状误差,图13为B2谱段狭缝显微视图,可以看到,刀口平直锐利,在全狭缝范围内无明显毛刺,宽度的实测结果(d_l)为 $14.992\mu\text{m}$,两刃口平行度误差不超过 $0.5\mu\text{m}$ 。

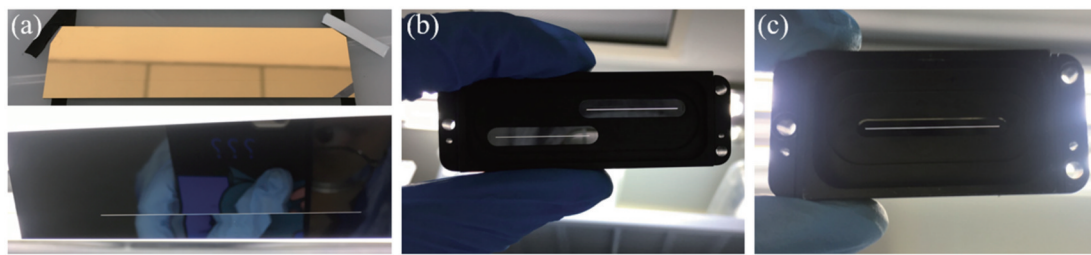


图12 硅基长狭缝。(a) B1、B2谱段狭缝,长61.44 mm、宽15 μm ;(b) B3、B4谱段狭缝,双缝拼接,总长49.16 mm、宽24 μm ;(c) B5谱段狭缝,长24.58 mm,宽24 μm

Fig. 12 Silicon long slits. (a) Slit for B1 and B2 bands with length of 61.44 mm and width of 15 μm ; (b) slit for B3 and B4 bands with length of 49.16 mm and width of 24 μm ; (c) slit for B5 band with length of 24.58 mm and width of 24 μm

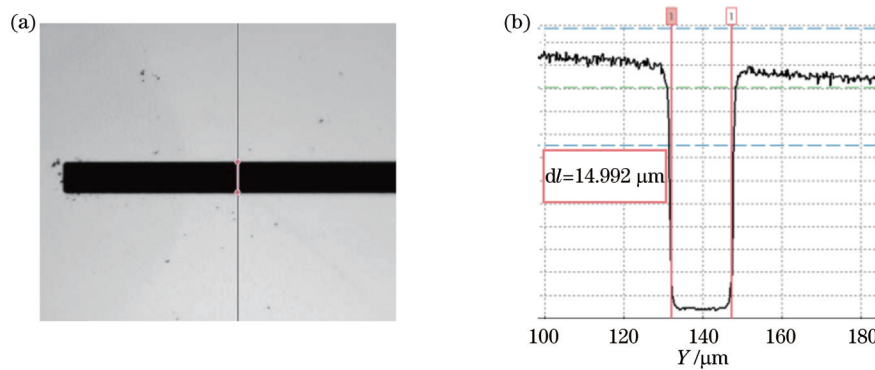


图13 B2谱段狭缝显微镜测试图。(a) 10 \times 显微放大图;(b)狭缝宽度测试结果
Fig. 13 Micrograph of slit for B2. (a) 10 \times micrograph; (a) test result of slit width

凸面闪耀衍射光栅是一种重要的分光元件,是分光系统的孔径光阑,其刻线、槽形、衍射效率、面形误差等直接影响分光系统的透过率、杂散光和波前差。GeoFWHIS分光系统中衍射光栅的特点在于槽密度低、闪耀角小,尤其在B5谱段,光栅槽密度仅为8.8 lp/mm,已突破全息记录光栅刻线密度的下限,因此要在凸面基底刻出大周期、小闪耀角的锯齿槽形十分困难。本实验采用光学系统与制造工艺联合设计方法,在满足设计指标的前提下优化光栅刻线、槽形等参数,使之满足当前精密微纳加工工艺的要求。所研制的各谱段闪耀光栅如图14所示,衍射效率曲线如图15所示。B1、B2谱段光栅直接刻于弯月镜表面,并在光栅区域镀反射膜,其他区域镀增透膜。各谱段光栅槽密度的测量值与设计值接近,误差不超过1%。槽形均为闪耀锯齿槽;闪耀角的测量值与设计值接近,槽顶角略偏离理想的直角,表现为钝角或圆角,该偏离将影响光栅峰值衍射效率,但各谱段仍有较高的效率,B1、B4、B5谱段峰值效率更是超过80%,最高达到86.4%。可见,所设计系统在满足指标要求的同时,还充分保证了分光系统的透过率和信噪比。

4.2 装调与测试

Offner和Wynne-Offner型分光系统在以MTF为

判据时通常有较大的装调公差范围,但以光谱畸变为判据时,凸面光栅和凹面反射镜对同轴度误差较敏感,尤其在本文所述的长狭缝分光系统中,对该误差的要求十分严格,离轴量须控制在0.01 mm以内,以保证小于10%像元的谱线弯曲和色畸变满足设计要求。为了实现高精度的光轴对准,自行研制了高精度点源显微镜^[59],如图16所示,用于确定球面镜的球心位置,以辅助分光系统装调。该显微镜的横向对准精度为0.4 μm ,轴向对准精度为1 μm 。点源显微镜在B1、B2谱段中,用于确定弯月镜-光栅和球面反射镜的相对位置;在B3谱段中,用于确定两分离弯月镜的相对位置、弯月镜与光栅的相对位置、弯月镜-光栅组件与球面反射镜的相对位置。图16(b)所示为利用点源显微镜监控B3谱段两块分离弯月镜球心位置的实验装置,调整弯月镜使两球心像尽量对准;图16(c)所示为点源显微镜显示的对准后的两球心位置,间隔为3.6 μm 。

采用全金属材料的Snap-together设计^[60-61]B4、B5谱段光机结构,最小化光学元件和结构件数量,减少零件间装配,以提高结构可靠性,缩短装调流程。每个光学元件与光机框架均设计配合基准,将装调过程中的公差要求前移到加工过程,基于单点金刚石车削的微米级形位误差,将光学元件的光学面与接口面在一次

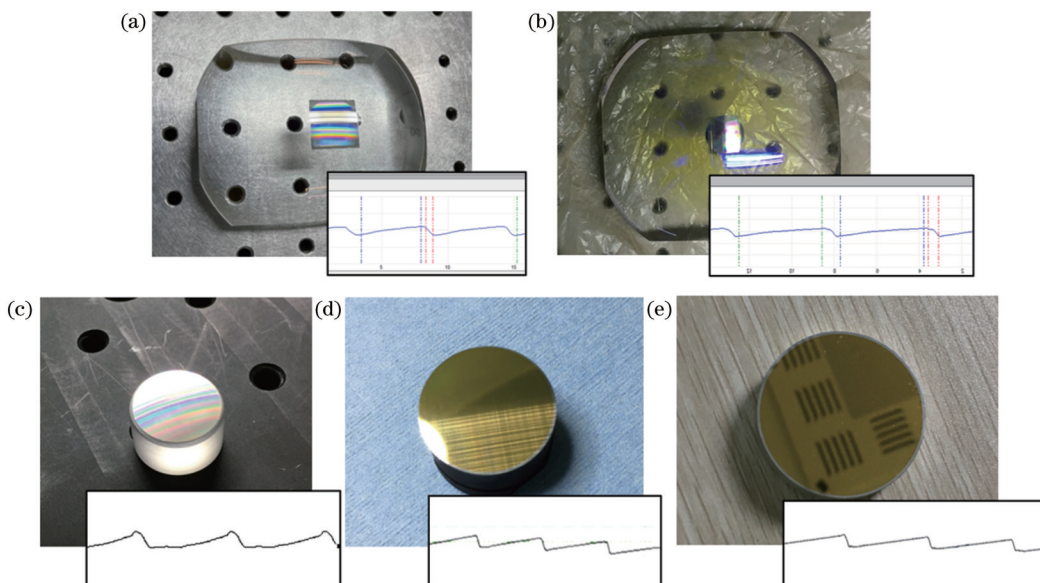


图14 凸面闪耀光栅与槽形测试形貌,右下角为原子力显微镜测得的槽形。(a) B1谱段,槽密度为312.1 lp/mm,闪耀角为3.8°;(b) B2谱段,槽密度为210.1 lp/mm,闪耀角为4.75°;(c) B3谱段,槽密度为68.5 lp/mm,闪耀角为3.1°;(d) B4谱段,槽密度为19.1 lp/mm,闪耀角为2.8°;(e) B5谱段,槽密度为8.8 lp/mm,闪耀角为2.8°

Fig. 14 Convex blazed gratings and their groove shapes, the lower right corner shows AFM test results of groove shapes. (a) B1 band, groove density is 312.1 lp/mm and blazed angle is 3.8°; (b) B2 band, groove density is 210.1 lp/mm and blazed angle is 4.75°; (c) B3 band, groove density is 68.5 lp/mm and blazed angle is 3.1°; (d) B4 band, groove density is 19.1 lp/mm and blazed angle is 2.8°; (e) B5 band, groove density is 8.8 lp/mm and blazed angle is 2.8°

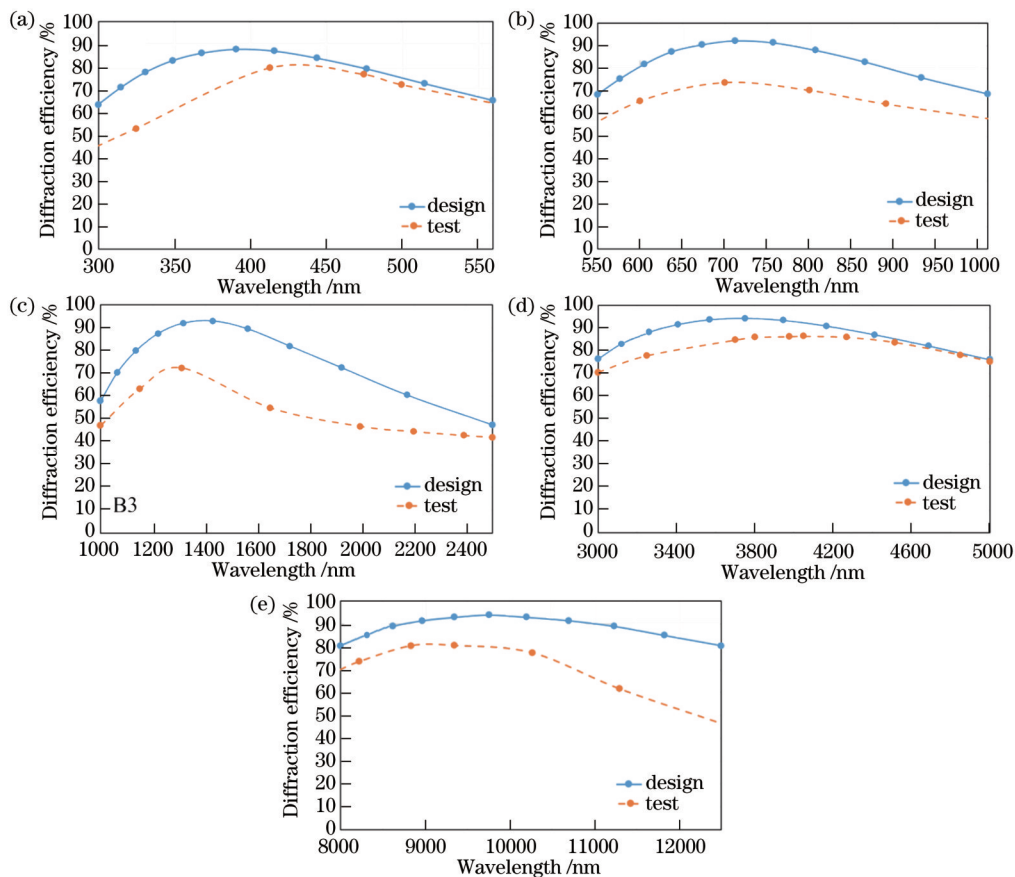


图15 B1~B5谱段的光栅衍射效率曲线。(a) B1谱段;(b) B2谱段;(c) B3谱段;(d) B4谱段;(e) B5谱段

Fig. 15 Diffraction efficiency curves of gratings at B1-B5 bands. (a) B1 band; (b) B2 band; (c) B3 band; (d) B4 band; (e) B5 band

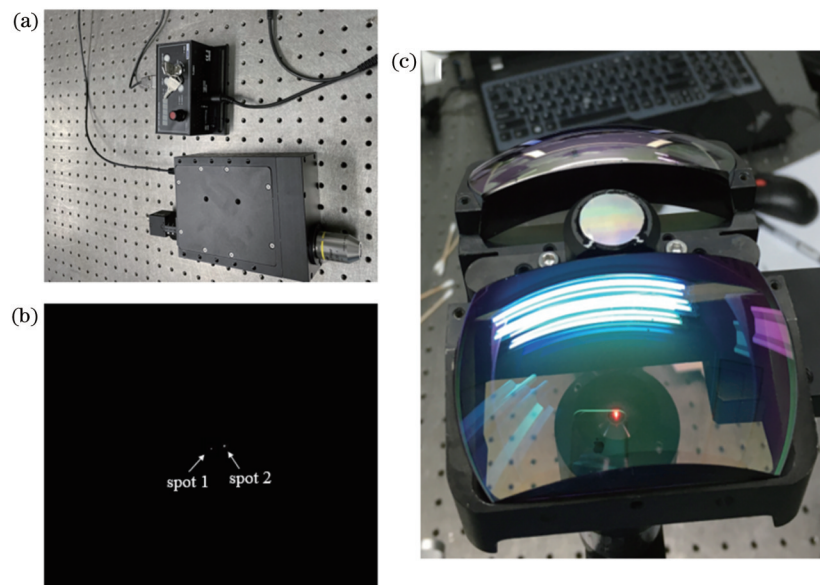


图 16 利用点源显微镜进行分光系统对心装调。(a)自研点源显微镜;(b)利用点源显微镜对准B3分光系统中两分离弯月镜的球心;
(c)点源显微镜视场内两球面星点像

Fig. 16 Alignment of the spectrometer by utilizing a point source microscope. (a) Self-developed point source microscope; (b) alignment of two separated meniscus in B3 spectrometer with point source microscope; (c) star images of two spherical surfaces in field of view of point source microscope

装夹中完成加工,结构件的装配面也在一次装夹中完成加工,实现微米级的装配间隙,保证系统只装不调即

可满足光学设计的公差要求。图 17 为装调完成的各谱段分光系统原理样机。

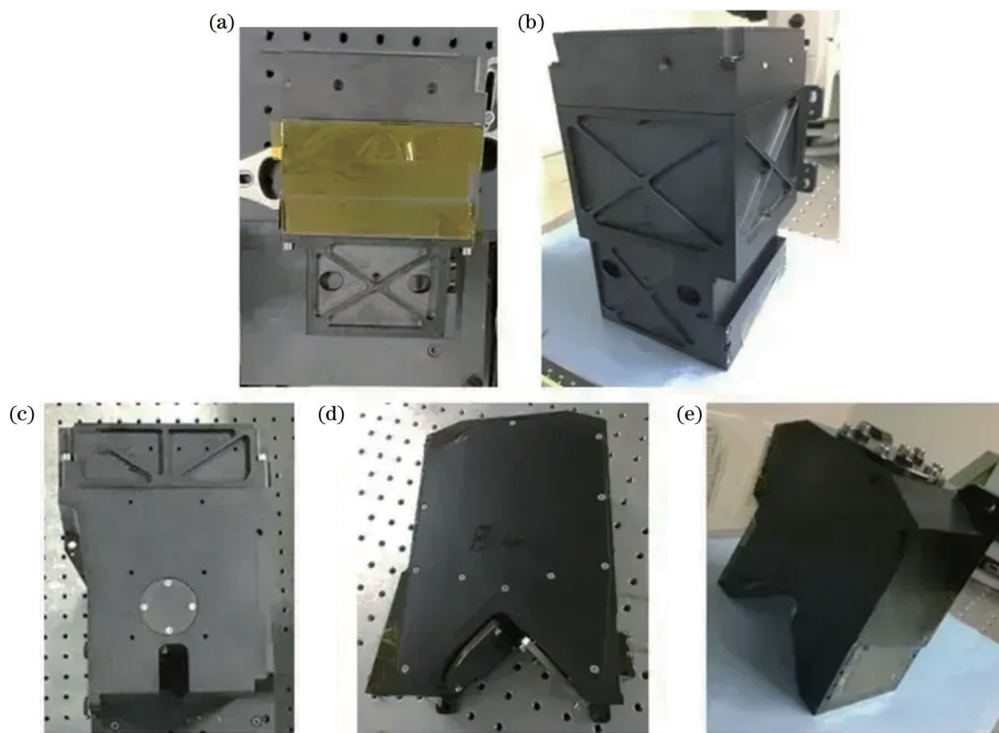


图 17 全谱段分光系统样机。(a) B1 谱段;(b) B2 谱段;(c) B3 谱段;(d) B4 谱段;(e) B5 谱段

Fig. 17 Full-spectrum spectrometer prototypes. (a) B1 band; (b) B2 band; (c) B3 band; (d) B4 band; (e) B5 band

以 B2 和 B5 谱段为例,介绍分光系统的测试结果。B2 谱段分光系统性能测试装置如图 18(a)所示,用汞镉灯均匀照射狭缝,用小像元 CCD 探测器采集光源特

征谱线,像元尺寸为 $5.5 \mu\text{m}$ 。测得的部分谱线如图 18(b)所示,分光系统工作谱段($0.55\sim1.01 \mu\text{m}$)内和谱段附近的谱线有 $546.1, 579.96, 579.07, 643.8 \text{ nm}$ 的

一级谱线和479.9、508.5 nm的二级谱线,二级谱线的成像路径与其两倍波长的一级光谱成像路径重合,可用于表现其两倍波长处的分光成像性能。求取这些谱线在光谱维的质心坐标,可以计算得到分光系统的线色散率为55.44 nm/mm,分光系统正常工作时所用的探测器像元尺寸为15 μm,将光谱维方向6个像元合并,

可计算得到像元合并后光谱采样间隔为4.99 nm,与设计值5 nm相当,且在整条狭缝范围保持一致。将垂直于谱线方向的能量分布拟合为高斯函数,结果如图18(c)所示,得到SRF曲线,其半峰全宽即为光谱分辨率,表7给出了分光系统在不同视场和不同波长处的光谱分辨率值,可以看出全谱面内光谱分辨率均匀分布。

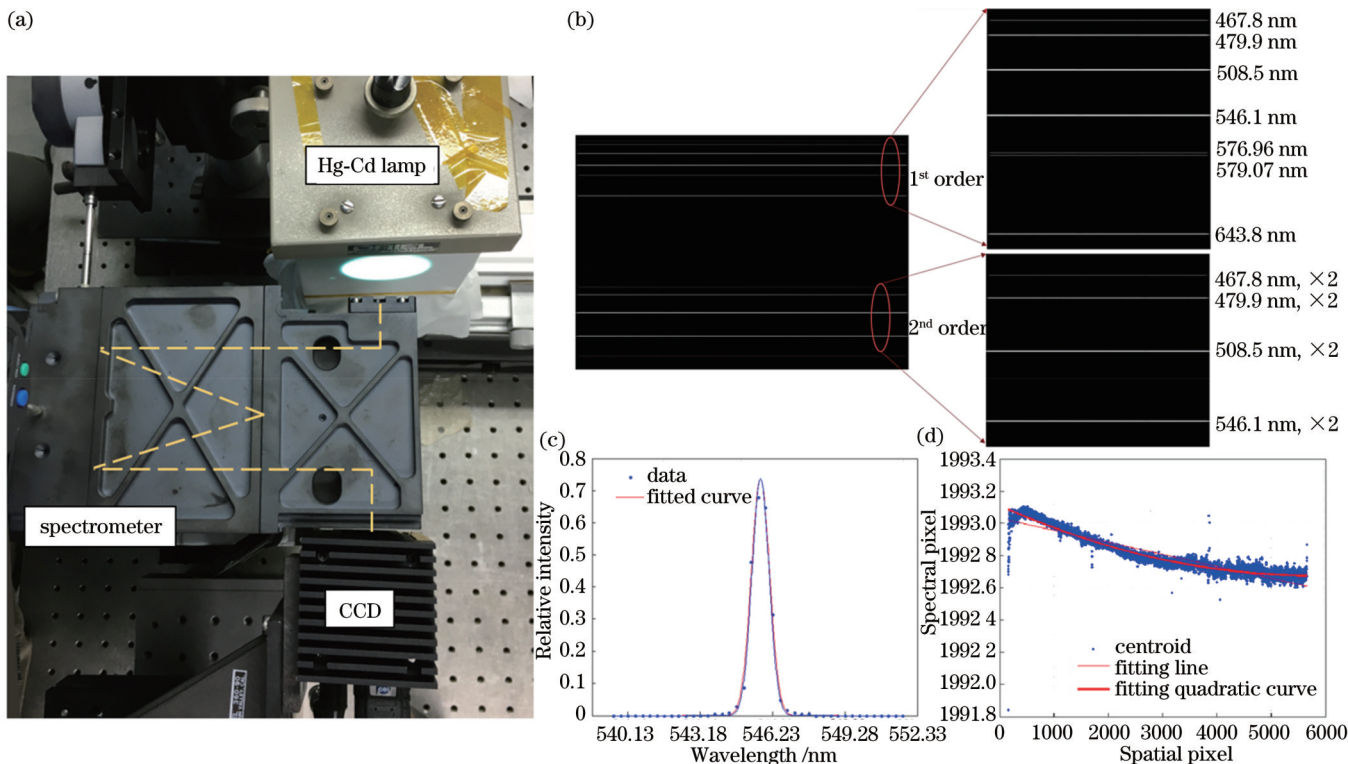


图18 B2谱段分光系统性能测试装置与结果。(a)光谱性能测试装置;(b)谱线图;(c)546.1 nm谱线的SRF;(d)546.1 nm谱线散点图与拟合曲线

Fig. 18 Test device and test results of B2 spectrometer. (a) Test device of spectral property; (b) spectral lines; (c) SRF of 546.1 nm spectral line; (d) scatter diagram of 546.1 nm spectral line and its fitting curve

表7 B2谱段分光系统的FWHM(光谱分辨率)
Table 7 FWHM (spectral resolution) of B2 spectrometer

Wavelength /nm	FWHM /nm					
	-1 field	-0.5 field	0 field	+0.5 field	+1 field	Average
546.1	5.02	5.01	4.99	4.99	5.01	5.01
643.8	5.02	5.02	5.02	5.00	5.01	5.02
959.8	5.02	5.00	5.02	5.02	5.02	5.02
1017	5.02	5.02	5.01	5.01	5.02	5.02

通过提取谱线散点图[图18(d)],计算特征谱线光谱维质心位置与理想质心位置的偏差,可计算得到谱线弯曲值。在所测谱线中546.1 nm谱线的弯曲最大,占3.3%个像元。利用宽带复色点光源从狭缝两端输入,分别采集位于狭缝两端的点色散线,计算色散线的斜率差值,可得到色畸变值,测试结果显示色畸变的最大值占2.3%个像元。同时,采用OPTIKOS光学性能综合测试系统测试了MTF,632.8 nm波长、33.3 lp/mm槽密度处的MTF测试值为0.76,接近衍

射极限。此外,采用大口径积分球作为照明光源,测试了分光系统的杂散光,空间维杂散光系数的测试结果为0.09%,光谱维杂散光系数的测试结果为0.45%。从测试结果可见,该分光系统在全谱面内的光谱均匀性高、光谱畸变小、成像质量高、杂散光含量低,具有高保真的分光成像性能。

B5谱段分光系统的性能测试装置如图19(a)所示,测试原理与B2谱段相同,在室温下,用高温(800 K)黑体结合窄带滤光片和聚光镜照射分光系统

狭缝，并用非制冷长波红外探测器接收谱线。测试采用的滤光片的波长分别为(8224±100) nm、(8834±105) nm、(9350±110) nm，测得的原始谱线和去除背景后的谱线如图19(b)所示。根据谱线光谱维质心坐标可计算出分光系统的线色散率为2052 nm/mm,3个像元合并时光谱采样间隔为197 nm。表8给出了由

SRF计算得到的光谱分辨率值，可以看出系统光谱分辨率比设计值200 nm稍有展宽，这是由长波红外衍射造成的。用与B2谱段相同的方法测试得到B5谱段分光系统的谱线弯曲最大值为2.8%个像元，色畸变值为3.6%个像元，均满足要求。

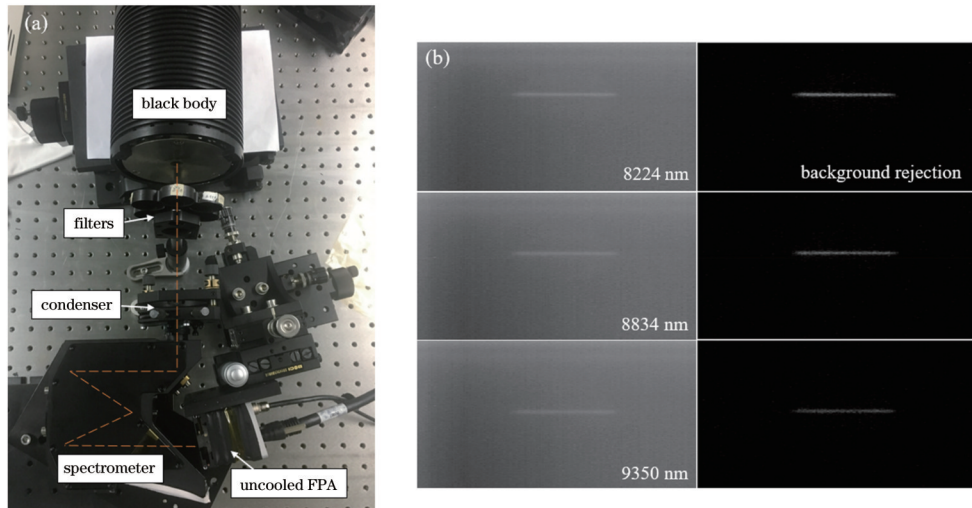


图19 B5谱段分光系统光谱性能测试装置与谱线图。(a)光谱性能测试装置；(b)谱线图

Fig. 19 Test device and spectral lines of B5 spectrometer. (a) Test device; (b) spectral lines

表8 B5谱段分光系统的FWHM(光谱分辨率)
Table 8 FWHM (spectral resolution) of B5 spectrometer

Wavelength / nm	FWHM / nm			
	-1 field	0 field	+1 field	Average
8224	201.3	201.0	200.9	201.1
8834	202.4	202.1	201.9	202.1
9350	205.9	204.9	204.2	205.0

5 总 结

分析设计了静止轨道全谱段宽覆盖成像光谱仪光学系统，该系统包含无焦望远系统、成像物镜、分光系统三部分，将0.3~12.5 μm的全谱段细分为B1(UVIS)、B2(VNIR)、B3(SWIR)、B4(MWIR)和B5(LWIR)5个子谱段集成于光学系统，实现了400 km幅宽、25~100 m空间分辨率和4~200 nm光谱分辨率。重点研究了高保真分光系统，根据其长狭缝和小体积的特点，采用Offner和Wynne-Offner装置设计各谱段分光系统，每个谱段均采用4个分光系统拼接来实现超长狭缝，狭缝总长最长达241.3 mm。对所设计系统的光学性能进行全方面评价，结果表明，该分光系统具备成像质量优、光谱畸变小、光谱响应均匀、杂散光低和信噪比高等高保真分光成像性能。研制了全谱段分光系统原理样机，给出了各谱段核心分光元件凸面闪耀光栅的研制结果，并以B2和B5谱段为例给出原理样机的装调测试过程。从测试结果来看，各谱段凸面光栅具有较理想的锯齿闪耀槽形和较高的衍射效

率，最高峰值效率达86.4%，原理样机各项指标测试值与设计值相符，具有高保真分光成像性能。所设计的GeoFWHIS光学系统为我国静止轨道全谱段高光谱遥感提供技术储备，全谱段高保真分光系统的成功研制验证了设计方案的可行性和正确性。

参 考 文 献

- [1] Vane G, Goetz A F H, Wellman J B. Airborne imaging spectrometer: a new tool for remote sensing[J]. IEEE Transactions on Geoscience and Remote Sensing, 1984, GE-22(6): 546-549.
- [2] Green R O, Eastwood M L, Sarture C M, et al. Imaging spectroscopy and the airborne visible/infrared imaging spectrometer (AVIRIS) [J]. Remote Sensing of Environment, 1998, 65(3): 227-248.
- [3] Lucey P G, Horton K A, Williams T J, et al. SMIFTS: a cryogenically cooled, spatially modulated imaging infrared interferometer spectrometer[J]. Proceedings of SPIE, 1993, 1937: 130-141.
- [4] Hall J L, Boucher R H, Buckland K N, et al. MAGI: a new high-performance airborne thermal-infrared imaging spectrometer for earth science applications[J]. IEEE Transactions on Geoscience and Remote Sensing, 2015, 53(10): 5447-5457.
- [5] Warren D W, Boucher R H, Gutierrez D J, et al. MAKO: a high-performance, airborne imaging spectrometer for the long-wave infrared[J]. Proceedings of SPIE, 2010, 7812: 78120N.
- [6] Mouroulis P, Van Gorp B, Green R O, et al. Portable remote imaging spectrometer coastal ocean sensor: design, characteristics, and first flight results[J]. Applied Optics, 2014, 53(7): 1363-1380.
- [7] Pearlman J, Carman S, Segal C, et al. Overview of the Hyperion imaging spectrometer for the NASA EO-1 mission

- [C]//IEEE 2001 International Geoscience and Remote Sensing Symposium (Cat. No.01CH37217), July 9-13, 2001, Sydney, NSW, Australia. New York: IEEE Press, 2001: 3036-3038.
- [8] Rast M, Bezy J L, Bruzzi S. The ESA medium resolution imaging spectrometer MERIS a review of the instrument and its mission[J]. International Journal of Remote Sensing, 1999, 20(9): 1681-1702.
- [9] Nieke J, Borde F, Mavrocordatos C, et al. The Ocean and Land Colour Imager (OLCI) for the Sentinel 3 GMES mission: status and first test results[J]. Proceedings of SPIE, 2012, 8528: 85280C.
- [10] Lucke R L, Corson M, McGlothlin N R, et al. Hyperspectral Imager for the coastal ocean: instrument description and first images[J]. Applied Optics, 2011, 50(11): 1501-1516.
- [11] Pan Q, Chen X H, Zhou J K, et al. Manufacture of the compact conical diffraction Offner hyperspectral imaging spectrometer[J]. Applied Optics, 2019, 58(27): 7298-7304.
- [12] Guanter L, Kaufmann H, Segl K, et al. The EnMAP spaceborne imaging spectroscopy mission for earth observation [J]. Remote Sensing, 2015, 7(7): 8830-8857.
- [13] 刘银年, 孙德新, 胡晓宁, 等. 高分五号可见短波红外高光谱相机设计与研制[J]. 遥感学报, 2020, 24(4): 333-344.
Liu Y N, Sun D X, Hu X N, et al. Development of visible and short-wave infrared hyperspectral imager onboard GF-5 satellite [J]. Journal of Remote Sensing, 2020, 24(4): 333-344.
- [14] Peschel T, Beier M, Damm C, et al. Integration and testing of an imaging spectrometer for earth observation[J]. Proceedings of SPIE, 2019, 11180: 111800.
- [15] Mourolis P, Green R O, Van Gorp B, et al. Landsat swath imaging spectrometer design[J]. Optical Engineering, 2016, 55(1): 015104.
- [16] Cogliati S, Sarti F, Chiarantini L, et al. The PRISMA imaging spectroscopy mission: overview and first performance analysis [J]. Remote Sensing of Environment, 2021, 262: 112499.
- [17] Lockwood R B, Cooley T W, Nadile R M, et al. Advanced responsive tactically effective military imaging spectrometer (ARTEMIS): system overview and objectives[J]. Proceedings of SPIE, 2007, 6661: 666102.
- [18] Zeng C B, Han Y, Liu B, et al. Optical design of a high-resolution spectrometer with a wide field of view[J]. Optics and Lasers in Engineering, 2021, 140: 106547.
- [19] Dwight J G, Tkaczyk T S, Alexander D, et al. Compact snapshot image mapping spectrometer for unmanned aerial vehicle hyperspectral imaging[J]. Journal of Applied Remote Sensing, 2018, 12(4): 044004.
- [20] Mu T K, Han F, Li H, et al. Snapshot hyperspectral imaging polarimetry with full spectropolarimetric resolution[J]. Optics and Lasers in Engineering, 2022, 148: 106767.
- [21] Bourdarot G, Le Coarer E, Bonfils X, et al. NanoVipa: a miniaturized high-resolution echelle spectrometer, for the monitoring of young stars from a 6U cubesat[J]. CEAS Space Journal, 2017, 9(4): 411-419.
- [22] Zhu J C, Shen W M. Analytical design of athermal ultra-compact concentric catadioptric imaging spectrometer[J]. Optics Express, 2019, 27(21): 31094-31109.
- [23] Chrisp M P, Lockwood R B, Smith M A, et al. Development of a compact imaging spectrometer form for the solar reflective spectral region[J]. Applied Optics, 2020, 59(32): 10007-10017.
- [24] Cook L G, Silny J F. Imaging spectrometer trade studies: a detailed comparison of the Offner-Chrisp and reflective triplet optical design forms[J]. Proceedings of SPIE, 2010, 7813: 78130F.
- [25] Yuan L Y, He Z P, Lv G, et al. Optical design, laboratory test, and calibration of airborne long wave infrared imaging spectrometer[J]. Optics Express, 2017, 25(19): 22440-22454.
- [26] Krimchansky A, Machi D, Cauffman S A, et al. Next-generation geostationary operational environmental satellite (GOES-R series): a space segment overview[J]. Proceedings of SPIE, 2004, 5570: 155-164.
- [27] 张鹏, 郭强, 陈博洋, 等. 我国风云四号气象卫星与日本Himawari-8/9卫星比较分析[J]. 气象科技进展, 2016, 6(1): 72-75.
Zhang P, Guo Q, Chen B Y, et al. The Chinese next-generation geostationary meteorological satellite FY-4 compared with the Japanese Himawari-8/9 satellites[J]. Advances in Meteorological Science and Technology, 2016, 6(1): 72-75.
- [28] Aminou D M A, Jacquet B, Pasternak F. Characteristics of the meteosat second generation (MSG) radiometer/imager: SEVIRI [J]. Proceedings of SPIE, 1997, 3221: 19-31.
- [29] Vaillon L, Schull U, Knigge T, et al. Geo-oculus: high resolution multi-spectral earth imaging mission from geostationary orbit[J]. Proceedings of SPIE, 10565: 105651V.
- [30] Elwell J D, Cantwell G W, Scott D K, et al. A geosynchronous imaging Fourier transform spectrometer (GIFTS) for hyperspectral atmospheric remote sensing: instrument overview and preliminary performance results[J]. Proceedings of SPIE, 2006, 6297: 62970S.
- [31] Tufillaro N, Davis C O, Valle T, et al. Behavioral model and simulator for the multi-slit optimized spectrometer (MOS) [J]. Proceedings of SPIE, 2013, 8870: 88700E.
- [32] Butz A, Orphal J, Checa-Garcia R, et al. Geostationary Emission Explorer for Europe (G3E): mission concept and initial performance assessment[J]. Atmospheric Measurement Techniques, 2015, 8(11): 4719-4734.
- [33] Choi W J, Moon K J, Yoon J, et al. Introducing the geostationary environment monitoring spectrometer[J]. Journal of Applied Remote Sensing, 2018, 12(4): 044005.
- [34] Polonsky I N, O'Brien D M, Kumer J B, et al. Performance of a geostationary mission, geoCARB, to measure CO₂, CH₄ and CO column-averaged concentrations[J]. Atmospheric Measurement Techniques, 2014, 7(4): 959-981.
- [35] Gulde S T, Kolm M G, Smith D J, et al. Sentinel 4: a geostationary imaging UVN spectrometer for air quality monitoring: status of design, performance and development[J]. Proceedings of SPIE, 2017, 10563: 1056341.
- [36] Zoogman P, Liu X, Suleiman R M, et al. Tropospheric emissions: monitoring of pollution (TEMPO) [J]. Journal of Quantitative Spectroscopy and Radiative Transfer, 2017, 186: 17-39.
- [37] 张以谋. 应用光学[M]. 4版. 北京: 电子工业出版社, 2015: 19.
Zhang Y M. Applied optics[M]. 4th ed. Beijing: Publishing House of Electronics Industry, 2015: 19.
- [38] Batshev V I, Puryaev D T. Geometrical and optical properties of an afocal two-mirror system[J]. Journal of Optical Technology, 2009, 76(1): 10-14.
- [39] Li Q, Han L, Jin Y M, et al. Afocal three-mirror anastigmat with zigzag optical axis for widened field of view and enlarged aperture[J]. Proceedings of SPIE, 2016, 10021: 100211T.
- [40] Hu B, Huang Y, Li Y. Design of four-mirror afocal principal system for wide field multichannel infrared imaging[J]. Proceedings of SPIE, 2015, 9618: 96180D.
- [41] Mouroulis P Z, McKerns M M. Pushbroom imaging spectrometer with high spectroscopic data fidelity: experimental demonstration[J]. Optical Engineering, 2000, 39(3): 808-816.
- [42] Mouroulis P, Green R O. Review of high fidelity imaging spectrometer design for remote sensing[J]. Optical Engineering, 2018, 57(4): 040901.
- [43] Kwo D, Lawrence G, Chrisp M. Design of a grating spectrometer from a 1:1 Offner mirror system[J]. Proceedings of SPIE, 1987, 0818: 275-281.
- [44] Prieto-Blanco X, Fuente R. Compact Offner-Wynne imaging spectrometers[J]. Optics Communications, 2014, 328: 143-150.
- [45] Zhu J C, Shen W M. Design and manufacture of compact long-slit spectrometer for hyperspectral remote sensing[J]. Optik,

- 2021, 247: 167896.
- [46] Reimers J, Bauer A, Thompson K P, et al. Freeform spectrometer enabling increased compactness[J]. Light: Science & Applications, 2017, 6(7): e17026.
- [47] Zhu J C, Chen X H, Zhao Z C, et al. Design and manufacture of miniaturized immersed imaging spectrometer for remote sensing [J]. Optics Express, 2021, 29(14): 22603-22613.
- [48] Montero-Orille C, Prieto-Blanco X, González-Núñez H, et al. Design of Dyson imaging spectrometers based on the Rowland circle concept[J]. Applied Optics, 2011, 50(35): 6487-6494.
- [49] van Gorp B, Mouroulis P, Wilson D W, et al. Design of the compact wide swath imaging spectrometer (CWIS) [J]. Proceedings of SPIE, 2014, 9222: 92220C.
- [50] Yu L. Upgrade of a UV-VIS-NIR imaging spectrometer for the coastal ocean observation: concept, design, fabrication, and test of prototype[J]. Optics Express, 2017, 25(13): 15526-15538.
- [51] Wu S, Huang C, Yu L, et al. Optical design and evaluation of an advanced scanning Dyson imaging spectrometer for ocean color[J]. Optics Express, 2021, 29(22): 36616-36633.
- [52] Prieto-Blanco X, Montero-Orille C, Couce B, et al. Analytical design of an Offner imaging spectrometer[J]. Optics Express, 2006, 14(20): 9156-9168.
- [53] 佟亚军, 吴刚, 周全, 等. Offner成像光谱仪的设计方法[J]. 光学学报, 2010, 30(4): 1148-1152.
- Tong Y J, Wu G, Zhou Q, et al. Design method of Offner-type imaging spectrometer[J]. Acta Optica Sinica, 2010, 30(4): 1148-1152.
- [54] 朱嘉诚, 陆伟奇, 赵知诚, 等. 静止轨道中波红外成像光谱仪分光成像系统[J]. 光学学报, 2021, 41(11): 1122001.
- Zhu J C, Lu W Q, Zhao Z C, et al. Spectroscopic imaging system in mid-wave infrared imaging spectrometer on geostationary orbit[J]. Acta Optica Sinica, 2021, 41(11): 1122001.
- [55] 朱嘉诚, 沈为民. 紧凑型消像散长狭缝光谱仪光学系统[J]. 红外与毫米波学报, 2019, 38(4): 542-548.
- Zhu J C, Shen W M. Compact anastigmatic long-slit spectrometer[J]. Journal of Infrared and Millimeter Waves, 2019, 38(4): 542-548.
- [56] Zhu J C, Chen X H, Zhao Z C, et al. Long-slit polarization-insensitive imaging spectrometer for wide-swath hyperspectral remote sensing from a geostationary orbit[J]. Optics Express, 2021, 29(17): 26851-26864.
- [57] 陈宇恒, 季铁群, 周建康, 等. 机载可见-红外超光谱成像仪信噪比的估算[J]. 红外与激光工程, 2012, 41(9): 2300-2303.
- Chen Y H, Ji Y Q, Zhou J K, et al. Signal-to-noise ratio evaluation of airborne visible-infrared hyperspectral imaging spectrometer[J]. Infrared and Laser Engineering, 2012, 41(9): 2300-2303.
- [58] Zhu J C, Zhao Z C, Shen S, et al. Analysis on NETD of thermal infrared imaging spectrometer[M]//Urbach H P, Yu Q F. 5th international symposium of space optical instruments and applications. Springer proceedings in physics. Cham: Springer, 2020, 232: 1-9.
- 杨拓拓, 陈新华, 赵知诚, 等. Offner分光成像系统的球面自准直法快速装调[J]. 中国光学, 2020, 13(6): 1324-1331.
- Yang T T, Chen X H, Zhao Z C, et al. Fast alignment of an Offner imaging spectrometer using a spherical autostigmatic method[J]. Chinese Optics, 2020, 13(6): 1324-1331.
- [59] Cobb J M, Comstock L E, Dewa P G, et al. Innovative manufacturing and test technologies for imaging hyperspectral spectrometers[J]. Proceedings of SPIE, 2006, 6233: 62330R.
- [60] Beier M, Hartung J, Peschel T, et al. Development, fabrication, and testing of an anamorphic imaging snap-together freeform telescope[J]. Applied Optics, 2015, 54(12): 3530-3542.
- [61] 1122001.

Design of Geostationary Full-Spectrum Wide-Swath High-Fidelity Imaging Spectrometer and Development of Its Spectrometers

Zhu Jiacheng^{1,2}, Zhao Zhicheng^{1,2}, Liu Quan^{1,2*}, Chen Xinhua^{1,2}, Li Huan³, Tang Shaofan³, Shen Weimin^{1,2**}

¹School of Optoelectronic Science and Engineering, Soochow University, Suzhou 215006, Jiangsu, China;

²Key Lab of Advanced Optical Manufacturing Technologies of Jiangsu Province & Key Lab of Modern Optical Technologies of Education Ministry of China, Soochow University, Suzhou 215006, Jiangsu, China;

³Beijing Institute of Space Mechanics and Electricity, Beijing 100094, China

Abstract

Objective It is necessary to develop full-spectrum hyperspectral remote sensing technology from geostationary orbit to fully meet the application requirements of continuous monitoring as well as fine identification and classification in the fields of disaster prevention and mitigation, environment, agriculture, forestry, ocean, meteorology, and resources. In view of the increasing demand for efficient and accurate spatial and spectral information acquisition, imaging spectrometers are driven to develop in the direction of faster response, larger width, higher resolution, and higher signal-to-noise ratio (SNR). Since the satellite in a geostationary orbit has the unique advantage of keeping relatively stationary with the ground, it has high timeliness and continuous observation capability and can obtain information from ground scenes quickly and widely. However, at present, most of the spectral remote sensing payloads serving on the geostationary orbit are multispectral payloads. They have only a dozen of spectral channels in the full spectrum, which is not sufficient to obtain fingerprint information of ground scenes, and their ability to identify types and components of substances is far inferior to that of hyperspectral payloads. The fusion with hyperspectral data in the full spectrum can greatly improve the recognition

accuracy and can provide more descriptions of targets. However, due to the great difficulty and high cost of such payloads, there is little related research reported at present. In this paper, we present an optical system of the geostationary full-spectrum wide-swath high-fidelity imaging spectrometer (GeoFWHIS). The prototypes of the spectrometers are developed to verify the correctness and feasibility of the design.

Methods According to the characteristics of the geostationary orbit, the imaging spectrometer covering near-ultraviolet to long-wave infrared (LWIR) is analyzed and designed. The full spectrum from $0.3\text{ }\mu\text{m}$ to $12.5\text{ }\mu\text{m}$ is divided into five sub-spectral bands and integrated into the optical system. Each sub-spectral band adopts four spectrometers to splice in the field of view to realize an ultra-long slit required for the wide width. The total length of the slit is 241.3 mm, and $400\text{ km} \times 400\text{ km}$ ground coverage is realized through internal scanning. The compact long-slit spectrometer meeting the splicing requirement is studied specifically. It is pointed out that low distortion, low stray light, high SNR, and uniform spectral response are the requirements for high-fidelity spectral imaging. The high-fidelity Offner and Wynne-Offner spectrometers based on convex-blazed gratings are designed. The performance of each part of the GeoFWHIS is fully evaluated, and the prototypes of each sub-spectral band are developed. Long slits for each band based on silicon substrate are developed by semiconductor technology, and the convex-blazed gratings are manufactured by holographic lithography and ion beam etching. The properties of the long slits and blazed gratings are tested and discussed. The alignment and test of the VNIR spectrometer and LWIR spectrometer are introduced as examples. In addition, we adjust the optical elements of spectrometers by using a high-precision point source microscope and achieve micrometer-level alignment precision. The performance that affects the fidelity of the spectrometers, such as MTF, spectral resolution, spectral distortions, and stray light, are tested and discussed.

Results and Discussions The optical system of GeoFWHIS is designed and evaluated. The design results show that its imaging quality is close to the diffraction limit in the full spectrum, and its spectral distortions, including the smile and keystone, are less than 1% pixel. The SNR of the system is also analyzed; the SNR of the B1 and B2 bands is higher than 250, and the SNR of the B3 band is higher than 150. Core elements of spectrometers are manufactured and tested. The results show that the maximum length of a single slit is 61.44 mm, and its width is only $15\text{ }\mu\text{m}$. The groove density of the gratings in five spectral bands ranges from 8.8 lp/mm to 312.1 lp/mm. The peak efficiency is all above 70%, and the maximum efficiency is 86.4%. The prototypes of the spectrometers are assembled and tested. The test results are consistent with the design results, which show high imaging quality, low distortion, low stray light, and uniform spectral response.

Conclusions The optical system of GeoFWHIS designed in this paper can realize hyperspectral imaging with a wide swath and a full spectrum. The full spectrum of $0.3\text{--}12.5\text{ }\mu\text{m}$ is divided into five sub-spectral bands, including UVIS, VNIR, SWIR, MWIR, and LWIR, which are integrated into the optical system to realize a swath of 400 km, spatial resolution of 25–100 m, and spectral resolution of 4–200 nm. The high-fidelity spectrometer is studied emphatically. The designed Offner and Wynne-Offner spectrometers can meet the requirements of a long slit and a small volume and have high imaging quality, low spectral distortion, uniform spectral response, low stray light, and high SNR. The prototypes of the spectrometers for each band are developed. The test results show that the convex-blazed grating has the desired sawtooth groove shape and high diffraction efficiency. The test results of the prototypes demonstrate high-fidelity performance, and all specifications meet the requirements. The GeoFWHIS reported in this paper provides a technical scheme for full-spectrum hyperspectral remote sensing from a geostationary orbit. The successful development of full-spectrum high-fidelity spectrometers verifies the feasibility and correctness of the design.

Key words optical design; imaging spectrometer; full-spectrum; high-fidelity; geostationary orbit; convex-blazed grating